AAS 25-773

HELIOCENTRIC MUTUALLY ORBITING GROUPS: PARAMETRIZATION, PHASING MANEUVERS, AND ORBITAL INSERTION

Jules Pénot* **and Hamsa Balakrishnan†**

This paper examines planar heliocentric Mutually Orbiting Groups (MOGs), satellite formations whose members revolve around a common virtual center as the group orbits the Sun. We parametrize these formations according to their semi-major axis, eccentricity, and number of satellites. We then derive fuel-optimal two-burn transfers for phasing maneuvers within a formation of arbitrary MOG parameters. We also analyze three orbital insertion strategies—Hohmann, one-burn, and spread-out—and examine the tradeoffs between their ΔV costs and times of flight. Using representative launch vehicle and satellite propulsion system performance values, we compute the achievable dry mass per satellite for each insertion strategy and set of MOG parameters. This work demonstrates the feasibility of the construction and reconfiguration of planar heliocentric MOGs of varying size, centered anywhere between the orbits of Mercury and Jupiter. This capability enables a wide range of MOG-based space systems, such as distributed astrophysics observatories, deep space navigation infrastructure, and interplanetary communication constellations.

INTRODUCTION

Over the last several decades, space missions have become increasingly distributed, with formation-flying groups or constellations of smaller spacecraft replacing large, monolithic satellites and probes.[1] These distributed space systems offer many advantages over their monolithic counterparts, including increased redundancy,[2] more frequent measurements increasing the effectiveness of Earth observation missions,[3] and more scalable Earth and interplanetary communications.[4] Such distributed space systems also enable entirely novel classes of missions that would have been infeasible with one or few spacecraft.

Satellites flying in a *formation* or *cluster*, unlike other types of constellations, maintain close proximity to each-other throughout their orbits. Satellites in a cluster are able to share resources such as data storage and down-link capacity,[5] make simultaneous measurements of the same target,[3,5] or ensure mission success even in the case of the total failure of an individual spacecraft.[6] A specific family of formation flying structures is the Mutually Orbiting Group (MOG)‡. MOG satellites all revolve around an imaginary "MOG center" in a quasi-elliptical formation, while the center itself revolves around the central gravitational body.

Some MOGs, referred to as *inclined MOGs*, have orbits that vary in their inclination and Right Ascension of the Ascending Node (RAAN), making them well-suited for Earth observation and other science missions. Examples of deployed or planned inclined MOGs include PIESAT-01,[5] the Laser Interferometer Space Antenna (LISA) mission,[7] and China's Taiji program.[8] By contrast, in a *planar MOG*, satellites are positioned in identical elliptical orbits that are staggered in their argument of periapsis and mean anomaly, such that all satellites lie in a plane that includes the central gravitational body. Figure 1 illustrates the example of a planar MOG, along with the satellites' full elliptical orbits. In the absence of external perturbations, neighboring

*Graduate Student, Department of Aeronautics and Astronautics, Massachusetts Institute of Technology, 77 Massachusetts Ave, Cambridge, MA 02139.

†William E. Leonhard (1940) Professor, Department of Aeronautics and Astronautics, Massachusetts Institute of Technology, 77 Massachusetts Ave, Cambridge, MA 02139.

‡Frequently-used symbols and abbreviations are listed alphabetically in the **Notation** section.

satellites in a planar MOG remain within a fixed distance range of each other. This behavior makes planar MOGs applicable to missions that need a stable cluster of formation-flying spacecraft, such as distributed space communication networks.[9]

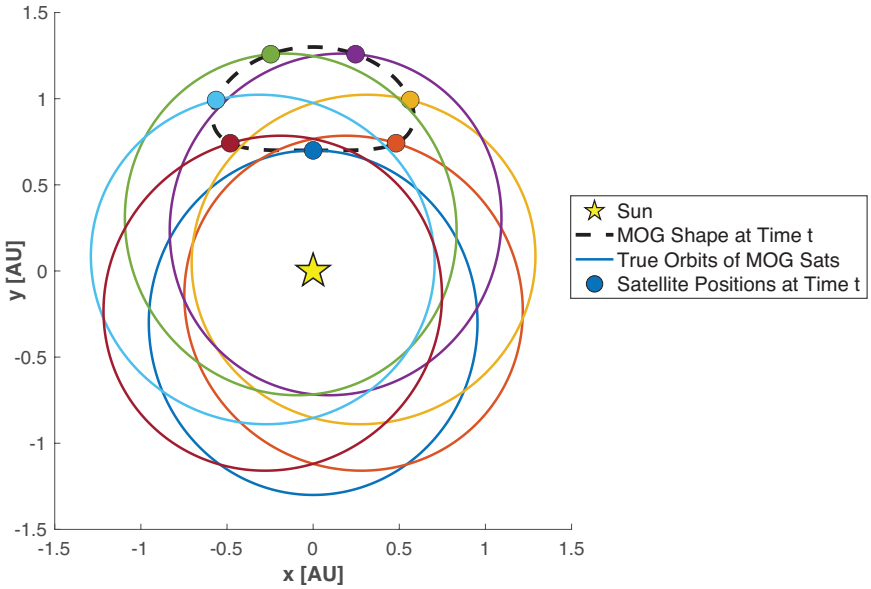

Figure 1: Illustration of a MOG with semi-major axis $a_{\mathrm{MOG}} = 1$ AU, eccentricity $e_{\mathrm{MOG}} = 0.3$, and $N_{\mathrm{sats}} = 7$ satellites, with the full elliptical orbits of the MOG satellites.

This paper addresses the construction, phasing and orbital insertion of satellites into *planar heliocentric MOGs*. Prior work on orbital insertion into heliocentric MOGs focused exclusively on the optimal insertion into a specific MOG.[7,10,11] By contrast, we adopt a parametric approach to the problem of insertion into planar heliocentric MOGs. Our approach therefore generalizes to any planar, heliocentric MOG of arbitrary size, number of satellites, and location in the Solar System.

PLANAR MOG PARAMETRIZATION

Definition and Construction

Each satellite in a Mutually Orbiting Group has the same orbital semi-major axis (a_{MOG}) and eccentricity (e_{MOG}), with staggered mean anomalies and arguments of periapsis. The number of satellites in the MOG is denoted by N_{sats}. Figure 2 illustrates the example of a 15-satellite MOG.

Consider the Keplerian orbital elements K_n, expressed in the J2000 ecliptic reference frame, of MOG satellite n at time t_0:

$$K_n = \begin{bmatrix} a_n \\ e_n \\ i_n \\ \Omega_n \\ \omega_n \\ \theta_{0,n} \end{bmatrix} = \begin{bmatrix} a_{\mathrm{MOG}} \\ e_{\mathrm{MOG}} \\ 0 \\ 0 \\ \omega_n \\ \theta_{0,n} \end{bmatrix} \tag{1}$$

In the above, i_n denotes the inclination, Ω_n denotes the RAAN, ω_n denotes the argument of periapsis, and $\theta_{0,n}$ denotes the initial true anomaly of satellite n's orbit.

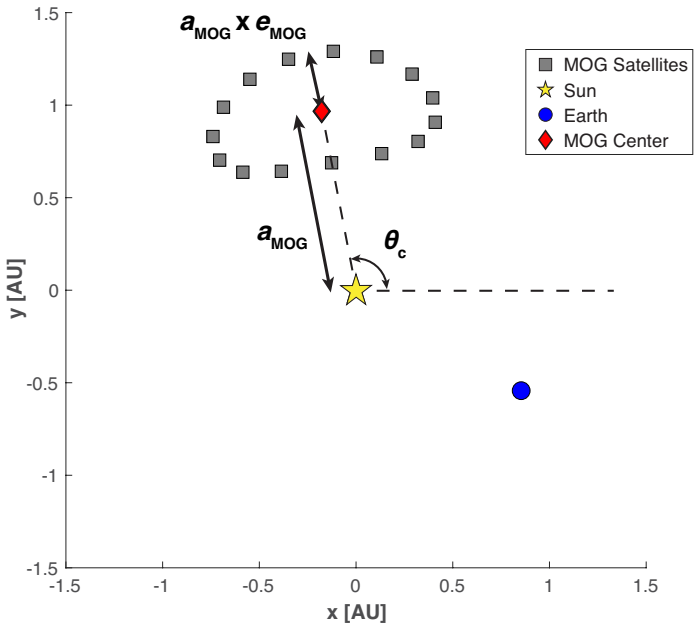

Figure 2: Mutually Orbiting Group with a_{MOG} = 1 AU, e_{MOG} = 0.3, and N_{sats} = 15.

Since the MOG preserves its structure along the entirety of the satellites' orbits, the ω_n need to be spread out uniformly over a 2π radian interval:

$$\omega_n = \omega_1 \ + \ (n-1) \ \cdot \frac{2\pi}{N_{\mathrm{sats}}} \tag{2}$$

where ω_1 is the argument of periapsis of MOG Satellite 1, which is also the true anomaly θ_{C} of the center of the MOG at time t_0, as depicted in Figure 2.

Due to this same symmetry requirement, the mean anomaly of satellite $n = 1, ..., N_{\mathrm{sats}}$ in its elliptical orbit at time t_0 must also be uniformly distributed over a 2π radian interval. A MOG is created by distributing these initial mean anomalies in the opposite direction to that of the ω_n distribution:

$$M_{0,n} = 2\pi \ - \ (n-1) \ \cdot \frac{2\pi}{N_{\mathrm{sats}}} \tag{3}$$

When constructed this way, it is clear that MOGs are a subfamily of the broader flower constellations, specifically 2D planar flower constellations in mean anomaly and argument of periapsis (M-ω flower constellations).[12] Planar MOGs are (1,1) M-ω flower constellations, but we could obtain the entire family of M-ω flower constellations by varying the relative size of the M and ω spacings between each satellite's orbital elements.

The relationship between an elliptical orbit's mean anomaly M and its true anomaly θ is given by the following transcendental equation, derived from Kepler's Equation:

$$M = \mathrm{atan2}[\sqrt{1-e^2} \cdot \sin(\theta), e + \cos(\theta)] \ - \ \frac{e \cdot \sqrt{1-e^2} \cdot \sin(\theta)}{1 + e \cdot \cos(\theta)} \tag{4}$$

where e is the orbit's eccentricity. We solve Equation (4) numerically to obtain the initial true anomaly of satellite n, namely, $\theta_{0,n}$.

MOG Profiles

An important observation is that the shape of the MOG formations depend only on the MOG eccentricity e_{MOG}, not its semi-major axis a_{MOG}. For all satellites in a MOG, all distances from both the MOG center and the Sun scale linearly with a_{MOG} for some fixed e_{MOG}. By contrast, increasing e_{MOG} deforms the MOG profile from an ellipse into a bean-shaped outline. The normalized MOG profiles for a range of MOG eccentricities are included in the appendix in Figure A1. For large e_{MOG}, the deformation of the MOG profile becomes significant enough to require a numerical approach for the design of optimal orbital insertion and phasing maneuvers.

MOG PHASING

MOG Anomaly and MOG Phase Definitions

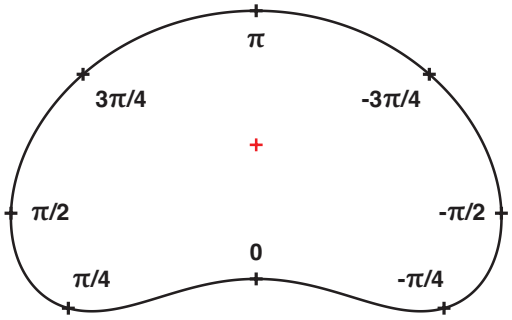

Figure 3: MOG Mean Anomaly M_{MOG} at different points in the MOG reference frame – MOG eccentricity e_{MOG} = 0.6. The MOG mean anomaly represents the evolution of a satellite's position within the MOG over time, and doesn't directly correspond to the physical angle of the satellite with respect to the MOG center.

We define the MOG mean anomaly M_{MOG} of a satellite in a MOG formation as the angle between the argument of periapsis ω of its real elliptical orbit around the Sun, and the true anomaly θ_{C} of the center of the MOG in its orbit around the Sun, as represented in Figure 2. Thus, as the MOG orbits around the Sun, or equivalently the MOG satellites orbit around the center of the MOG, M_{MOG} increases linearly in time from 0 to 2π. As represented in Figure 3, M_{MOG} increases as the satellites travel clockwise in the MOG frame, with $M_{\mathrm{MOG}} = 0$ corresponding to the elliptical orbit's periapsis and $M_{\mathrm{MOG}} = \pi$ corresponding to the apoapsis.

Let's define the MOG phase ϕ_{MOG} of a MOG satellite as the initial MOG mean anomaly M^0_{MOG} of that satellite. Defined as such, $\phi_{\mathrm{MOG}} = \omega_n$ for satellite n, where ω_n is the argument of periapsis of satellite n's orbit around the Sun as defined in equation (2).

The phase ϕ_{MOG} of a given satellite in a MOG is fixed in time in the absence of external perturbations. ϕ_{MOG} serves as a measure of the position of a satellite within the MOG relative to other MOG satellites. Notably, the difference in MOG anomaly M_{MOG} between two satellites (e.g., satellites 1 and 2) is the same as the difference between their MOG phases:

$$\begin{aligned}\Delta M_{\mathrm{MOG}}(t) &= M_{\mathrm{MOG2}}(t) - M_{\mathrm{MOG1}}(t) \\ &= (M^0_{\mathrm{MOG2}} + \frac{t - t_0}{T_{\mathrm{MOG}}} \cdot 2\pi) - (M^0_{\mathrm{MOG1}} + \frac{t - t_0}{T_{\mathrm{MOG}}} \cdot 2\pi) \\ &= \phi_{\mathrm{MOG2}} - \phi_{\mathrm{MOG1}} = \Delta\phi\end{aligned} \tag{5}$$

where $T_{\mathrm{MOG}} = 2\pi\sqrt{a^3_{\mathrm{MOG}}/\mu_{\mathrm{sun}}}$ is the orbital period of the MOG satellites around the Sun, and μ_{sun} is the Sun's standard gravitational parameter.

Problem Statement

The repositioning of individual satellites within the overall MOG formation arises in several operational scenarios, such as:

- Reconfiguration of the MOG formation to accommodate the insertion of new satellites into the MOG.
- Reconfiguration of the MOG formation to accommodate the failure of existing MOG satellites.
- MOG orbital insertion strategies that involve MOG phase change maneuvers.

We will assess the feasibility of such phase-change operations by computing the ΔV required to change the MOG phase of a satellite by some $\Delta\phi_{\mathrm{MOG}}$ in a MOG of given a_{MOG} and e_{MOG}.

Methodology

Finding fuel-optimal impulsive maneuvers for MOG phases changes is a non-trivial problem because changing the MOG phase of a satellite involves changing both the argument of periapsis ω and the mean anomaly M of the satellite's elliptical orbit. It is feasible to first execute a change in argument of periapsis maneuver followed by a mean-anomaly change maneuver, but we expect such an approach to be exceptionally expensive in ΔV and have a long time of flight. Instead, we calculate the fuel-optimal 2-burn maneuver that changes both ω and M simultaneously. This paper assumes that MOG satellites only use impulsive maneuvers for phase change maneuvers. Low-thrust propulsion phase-change maneuvers are outside the scope of this paper, but may be examined in future work.

For a given MOG constellation and desired MOG phase change $\Delta\phi_{\mathrm{MOG}}$, the nonlinear optimization problem objective is as follows:

$$\min_{(t_1,t_2)\in\mathbb{R}^2_+} (\Delta V(t_1, t_2, \Delta\phi_{\mathrm{MOG}}))$$

where t_1 is the time at which the MOG satellite enters its transfer orbit with a first burn, and t_2 is the time at which it arrives at its new position in the MOG, inserting into its final orbit with a second burn.

Algorithm 1 Computing ΔV from t_1, t_2, and $\Delta\phi_{\mathrm{MOG}}$

Input: Maneuver times t_1, t_2, phase offset $\Delta\phi_{\mathrm{MOG}}$. MOG parameters a_{MOG} and e_{MOG}.

Output: Total ΔV expended

$K_1 \leftarrow [a_{\mathrm{MOG}}, e_{\mathrm{MOG}}, 0, 0, 0, 0]^T$
$K_2 \leftarrow$ shiftKeplerianInMOG$(K_1, \Delta\phi_{\mathrm{MOG}})$
$K_1' \leftarrow$ propagateTrueAnomaly(K_1, t_1)
$K_2' \leftarrow$ propagateTrueAnomaly(K_2, t_2)
$X_1 \leftarrow$ Keplerian2Cartesian(K_1')
$X_2 \leftarrow$ Keplerian2Cartesian(K_2')
$R_1 \leftarrow X_1(1:3)$ {(x,y,z) coordinates of starting MOG position}
$R_2 \leftarrow X_2(1:3)$ {(x,y,z) coordinates of arrival MOG position}
$TOF \leftarrow t_2 - t_1$ {Maneuver time of flight}
$m \leftarrow 0$ {Number of full orbits around the Sun allowed in the Lambert solution}
$(V_1, V_2) \leftarrow$ lambert$(R_1, R_2, TOF, m, \mu_{\mathrm{sun}})$
$\Delta V_1 \leftarrow \|V_1 - X_1(4:6)\|$
$\Delta V_2 \leftarrow \|V_2 - X_2(4:6)\|$
$\Delta V \leftarrow \Delta V_1 + \Delta V_2$

To compute the ΔV for any given (t_1, t_2, $\Delta\phi_{\mathrm{MOG}}$), we employ the procedure described in Algorithm 1, where *lambert()* is the Lambert solver developed by Rody Oldenhuis,[13] based on the work of Izzo,[14]

Lancaster & Blanchard,[15] and Gooding.[16] We propagate the mean anomaly M linearly over time, and convert it to the true anomaly θ by solving Equation (4), obtaining the candidate phase-change maneuver start and end locations in Keplerian coordinates, K_1' and K_2'.

The ΔV function outlined in Algorithm 1 is nonlinear in t_1 and t_2 and non-convex, but it is smooth and well-defined except for near-zero time flights where the ΔV diverges. To find the global minimum of $\Delta V(t_1, t_2, \Delta\phi_{\mathrm{MOG}})$ w.r.t. t_1, t_2, we first discretize t_1 and t_2 in the interval $[0, 2 \cdot T_{\mathrm{MOG}}]$. We selected a minimum time of flight $TOF_{\min} = 0.2 \cdot T_{\mathrm{MOG}}$ since $\Delta V()$ diverges when $t_2 - t_1$ is small. The maximum time of flight, $TOF_{\max} = 0.9 \cdot T_{\mathrm{MOG}}$ was selected as a reasonable upper bound on the duration of phasing maneuvers. Longer phasing maneuvers, involving full orbits around the Sun, lead to only marginally-lower ΔVs and would be undesirable due to longer reconfiguration delays.

$$TOF_{\min} \leq t_2 - t_1 \leq TOF_{\max} \tag{6}$$

We first compute ΔV from Algorithm 1 for all t_1, t_2 pairs that comply with the linear constraint summarized in Equation (6). We then use the best t_1, t_2 as the initial guess for a local, nonlinear programming solver, MATLAB's *fmincon*(). *fmincon* returns the local minimum of $\Delta V(t_1, t_2)$ near this initial guess – so long as the resolution of the global t_1, t_2 search is fine enough, we would expect the final ΔV to be the global optimum within the bounds place on t_1 and t_2. We found that a resolution of 100 samples per orbit was sufficient to reliably identify the global optimum.

Results

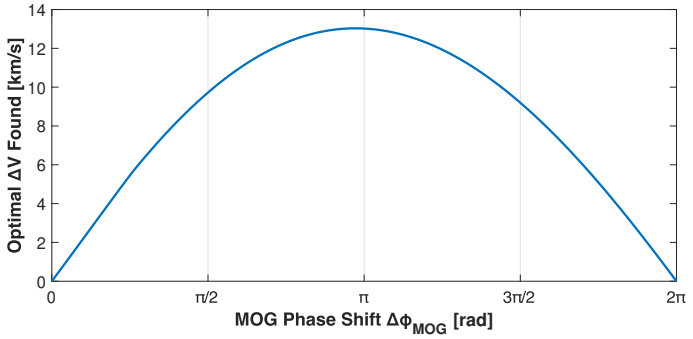

Figure 4: Phase Change ΔV as a function of $\Delta\phi_{\mathrm{MOG}}$ for a_{MOG} = 1.25 AU and e_{MOG} = 0.3.

We plot the results of the MOG phase change analysis in Figure 4 for a_{MOG} = 1.25 AU and e_{MOG} = 0.3. For a given MOG, $\Delta V(\Delta\phi_{\mathrm{MOG}})$ is nearly a parabola, with a maximum near $\Delta\phi_{\mathrm{MOG}} = \pi$. This makes physical sense, as changing a MOG satellite's ϕ_{MOG} by π radians involves completely inverting its elliptical orbit around the Sun (change of argument of periapsis of π) and a large true anomaly change of $-\pi$ radians. The parabola isn't perfectly symmetrical around $\Delta\phi_{\mathrm{MOG}} = \pi$ because the ΔV needed to reduce ϕ_{MOG} by some $-\Delta\phi_{\mathrm{MOG}}$ differs from that needed to increase ϕ_{MOG} by $\Delta\phi_{\mathrm{MOG}}$.

Large MOG phase changes are expensive in ΔV, making a complete MOG reconfiguration unrealistic for impulsive propulsion systems. Let's instead consider the ΔV cost of making small changes to the ϕ_{MOG} of a satellite in a given MOG parametrized by (a_{MOG}, e_{MOG}), a useful metric for evaluating the cost of small tweaks to a satellite's position in a MOG.

For each a_{MOG}, e_{MOG}, we linearize the leading and trailing edges of the $\Delta V(\Delta\phi_{\mathrm{MOG}})$ parabola to extract the ΔV cost per radian for small positive and negative MOG phase changes. The RMSEs of such a fit for the distribution represented in Figure 4 over the [0, 1 rad] range (small positive MOG phase changes) and [-1 rad, 0] range (small negative phase changes) are small, at 0.046 km/s and 0.083 km/s respectively.

We then compute the slopes of these linearizations, α_+ and α_-, for a range of e_{MOG}, a_{MOG} of interest. The results are presented in Figure 5. Note that the trailing edge slope, α_-, is taken as positive in this analysis,

since we are more interested in the magnitude of the ΔV required for phase changes than the direction in which thrusters must fire.

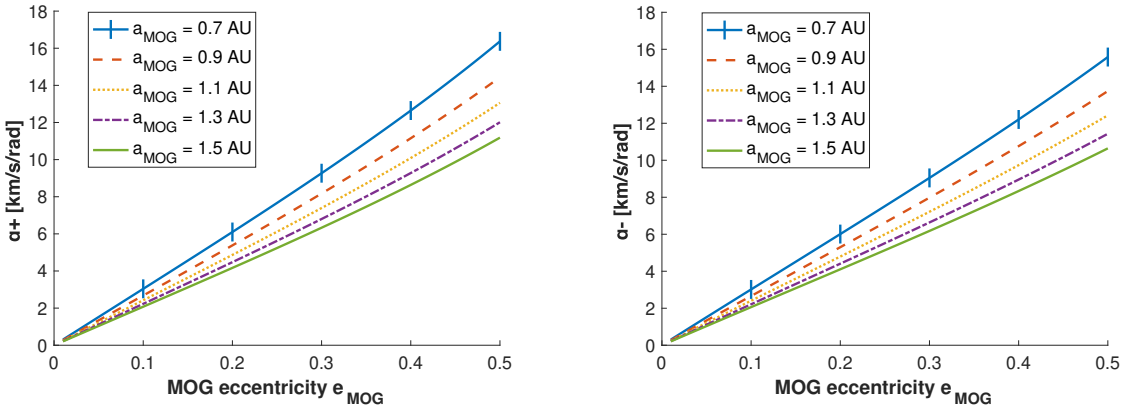

Figure 5: ΔV cost to make small ϕ_{MOG} adjustments, positive (α_+) and negative (α_-)

We perform a 2D fit on the $\alpha_+(e_{\text{MOG}}, a_{\text{MOG}})$ and $\alpha_-(e_{\text{MOG}}, a_{\text{MOG}})$ data, revealing that the only dependence of α_+, α_- on a_{MOG} is a factor of $\frac{1}{\sqrt{a_{\text{MOG}}}}$. This is consistent with the scaling of the MOG phasing problem – all distances in the geometry of a given MOG scale linearly with a_{MOG}, and the orbital velocity $\vec{v}_\theta$ at some given true anomaly θ in an elliptical orbit scales with $1/\sqrt{a}$ as the semi-major axis a is independently varied.

Therefore our expressions for $\alpha_+(e_{\text{MOG}}, a_{\text{MOG}})$, $\alpha_-(e_{\text{MOG}}, a_{\text{MOG}})$ are separable as follows:

$$\alpha_+(e_{\text{MOG}}, a_{\text{MOG}}) = \alpha_+(e_{\text{MOG}}) \cdot \sqrt{\frac{1\ [\text{AU}]}{a_{\text{MOG}}}} \tag{7}$$

$$\alpha_-(e_{\text{MOG}}, a_{\text{MOG}}) = \alpha_-(e_{\text{MOG}}) \cdot \sqrt{\frac{1\ [\text{AU}]}{a_{\text{MOG}}}} \tag{8}$$

where $\alpha_+(e_{\text{MOG}})$ and $\alpha_-(e_{\text{MOG}})$ are defined at a_{MOG} = 1 AU, and a_{MOG} is in AU.

We can approximate $\alpha_+(e_{\text{MOG}})$ and $\alpha_-(e_{\text{MOG}})$ using 3rd degree polynomials of the form:

$$p(e_{\text{MOG}}) = a \cdot e_{\text{MOG}}^3 + b \cdot e_{\text{MOG}}^2 + c \cdot e_{\text{MOG}} + d$$

We fix d = 0 to enforce the constraint that $\lim_{e_{\text{MOG}} \to 0}(\alpha_+(e_{\text{MOG}}))$ = $\lim_{e_{\text{MOG}} \to 0}(\alpha_-(e_{\text{MOG}}))$ = 0. The coefficients and figures of merit of these fits are summarized in Table 1. The figures of merit were computed by comparing the numeric approximation defined above to the results of the phasing maneuver optimization outlined in the **Methods** subsection. This comparison was carried out over the ranges $a_{\text{MOG}} \in [0.7, 1.5]$ AU and $e_{\text{MOG}} \in [0.01, 0.5]$, because these are the ranges of MOG parameters for which planar MOGs are most likely to have near-term applications such as LISA,[11] Taiji,[8] and distributed Earth-Mars communications.

Table 1: Polynomial fit coefficients and goodness of fit metrics for $\alpha_+(e_{\text{MOG}})$ and $\alpha_-(e_{\text{MOG}})$

Function	a (km/s)	b (km/s)	c (km/s)	RMSE (m/s/rad)	RMSE (%)	MAE (m/s/rad)	MAE (%)
α_+	15.1323	-4.4752	25.8481	9.7	0.15	9.2	0.14
α_-	10.8756	-4.5272	25.6050	1.7	0.03	1.4	0.02

Thus we can express the marginal ΔV cost of small positive and negative MOG phase changes, α_+ and α_-, as follows:

$$\alpha_+(a_{\mathrm{MOG}}, e_{\mathrm{MOG}}) = (a^+ \cdot e_{\mathrm{MOG}}^3 + b^+ \cdot e_{\mathrm{MOG}}^2 + c^+ \cdot e_{\mathrm{MOG}}) \cdot \frac{1}{\sqrt{a_{\mathrm{MOG}}}}$$

$$\alpha_-(a_{\mathrm{MOG}}, e_{\mathrm{MOG}}) = (a^- \cdot e_{\mathrm{MOG}}^3 + b^- \cdot e_{\mathrm{MOG}}^2 + c^- \cdot e_{\mathrm{MOG}}) \cdot \frac{1}{\sqrt{a_{\mathrm{MOG}}}}$$

where (a^+, b^+, c^+) and (a^-, b^-, c^-) are the coefficients from the polynomial fits of α_+ and α_- respectively, presented in Table 1.

MOG ORBITAL INSERTION

Problem Statement

The study of the orbital insertion of satellites into planar, heliocentric MOGs is critical to establishing the feasibility of their construction. We propose and analyze three main strategies for inserting satellites into a MOG of some semi-major axis a_{MOG} and eccentricity e_{MOG}.

Hohmann Insertion from a Circular Orbit

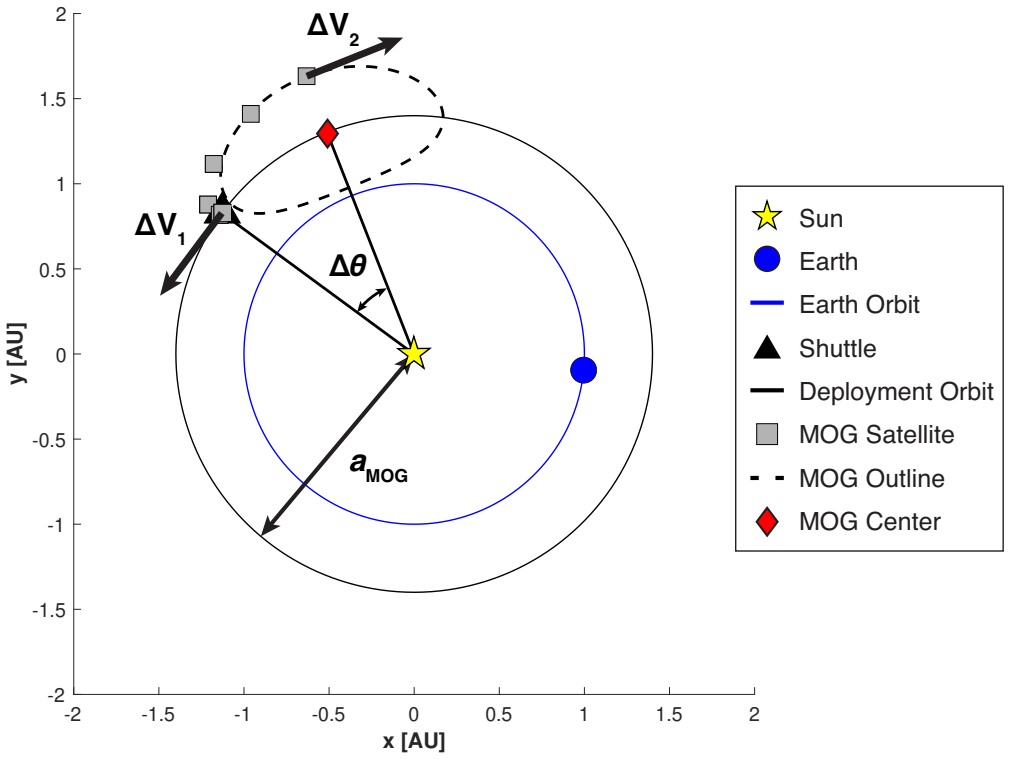

Figure 6: Hohmann insertion procedure for MOG satellite insertion from a circular orbit of radius a_{MOG}. Satellites enter the Shuttle $\rightarrow$ MOG transfer orbit at regular time intervals $\Delta t = T_{\mathrm{MOG}}/N_{\mathrm{sats}}$ by executing a first burn of magnitude ΔV_1. They then insert some time of flight later (TOF) into their MOG orbits with a second burn of magnitude ΔV_2.

Let us consider the following MOG orbital insertion procedure for a MOG of parameters a_{MOG}, e_{MOG}:

1. MOG satellites launch aboard some launch vehicle, entering a LEO parking orbit

2. A common bus (the "shuttle") containing the satellites (e.g., Starship upper stage) carries out burns to exit LEO, carrying out a Hohmann transfer to a circular orbit of radius a_{MOG}

3. Over the course of a full revolution of the bus and MOG around the Sun, the satellites detach from the bus and each carry out a fuel-optimal 2-burn transfer into an elliptical orbit of semi-major axis a_{MOG} and eccentricity e_{MOG}

We will refer to step 3 of the above procedure as the "fuel-optimal 2-burn insertion" or "Hohmann Insertion" procedure. As represented in Figure 6, this procedure involves placing these satellites one-by-one into an elliptical orbit of semi-major axis a_{MOG}, eccentricity e_{MOG}, and argument of periapsis ω offset a constant $\Delta\theta$ from the shuttle's current true anomaly $\theta_{\mathrm{shuttle}}$. If the satellites are inserted into these elliptical orbits at regular time intervals of $\Delta t = T_{\mathrm{MOG}}/N_{\mathrm{sats}}$, then they naturally form a planar Sun-orbiting MOG of parameters (a_{MOG}, e_{MOG}) as desired. Note that this orbital insertion strategy is only possible if the shuttle is on a circular orbit of radius R = a_{MOG}, hence the initial Hohmann transfer from Earth's orbit around the Sun to the satellite deployment orbit.

Identifying the fuel-optimal satellite insertion transfer corresponds to finding the optimal 2-burn transfer from a circular orbit to a coplanar elliptical orbit of same semi-major axis. Since those two orbits are coplanar and have the same semi-major axis, the Hohmann transfer is the globally optimal transfer between those two orbits.[17]

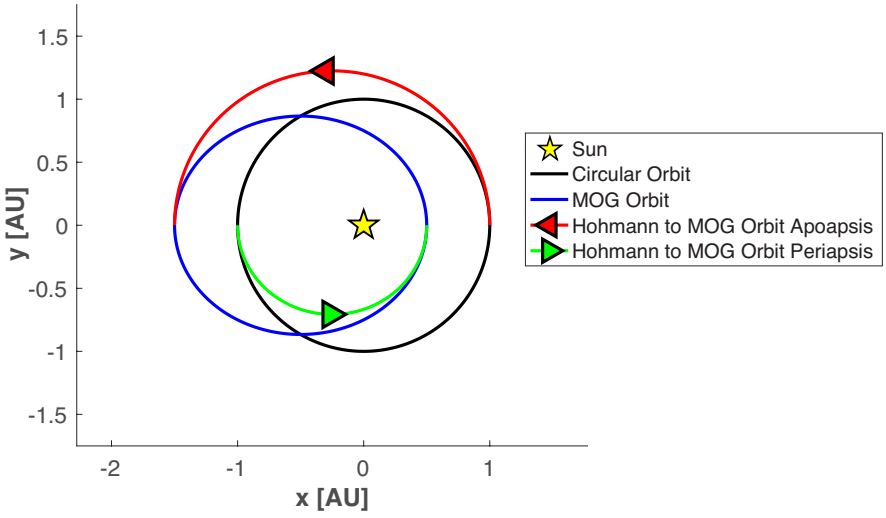

Figure 7: Candidate Hohmann Transfers for 2-Burn MOG Insertion for a_{MOG} = 1 AU, e_{MOG} = 0.5.

Hohmann transfers between co-planar, co-axial ellipses are always between the apsides of said ellipses.[17] Since one of our terminal orbits is circular, this narrows down the possible globally-optimal transfer to two possible Hohmann transfers, which we plot in Figure 7: one transfer that inserts the satellite at the MOG elliptical orbit's aphelion, and another that inserts the satellite at the perihelion.

We express the total ΔV required for each Hohmann transfer as a function of a_{MOG} and e_{MOG}, using the ΔV formulae originally developed by Hohmann in his 1925 paper and the vis-viva equation.[18]

$$\Delta V_{\mathrm{a}} = |\Delta V_{1\mathrm{a}}| + |\Delta V_{2\mathrm{a}}| = \sqrt{\frac{\mu_{\mathrm{sun}}}{a_{\mathrm{MOG}}}} \cdot \left(\sqrt{1 + \frac{e_{\mathrm{MOG}}}{2 + e_{\mathrm{MOG}}}} - 1 + \sqrt{\frac{2}{1 + e_{\mathrm{MOG}}} - \frac{2}{2 + e_{\mathrm{MOG}}}} - \sqrt{\frac{2}{1 + e_{\mathrm{MOG}}} - 1}\right) \tag{9}$$

$$\Delta V_{\mathrm{p}} = |\Delta V_{1\mathrm{p}}| + |\Delta V_{2\mathrm{p}}| = \sqrt{\frac{\mu_{\mathrm{sun}}}{a_{\mathrm{MOG}}}} \cdot \left(1 - \sqrt{1 - \frac{e_{\mathrm{MOG}}}{2 - e_{\mathrm{MOG}}}} - \sqrt{\frac{2}{1 - e_{\mathrm{MOG}}} - \frac{2}{2 - e_{\mathrm{MOG}}}} + \sqrt{\frac{2}{1 - e_{\mathrm{MOG}}} - 1}\right) \tag{10}$$

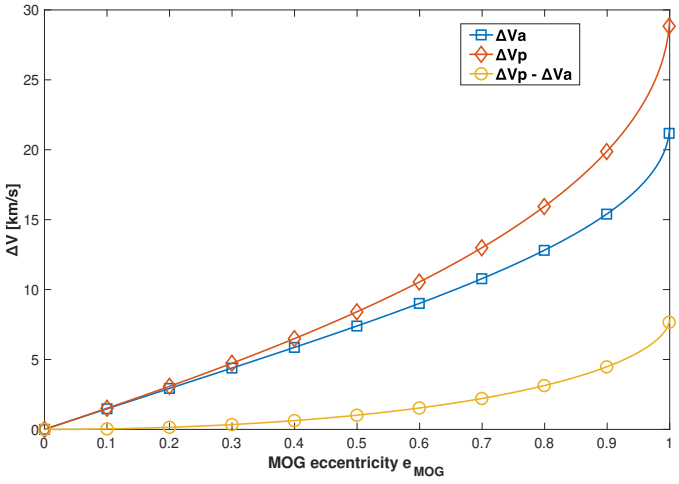

Figure 8: $\Delta V_{\mathrm{a}}(e_{\mathrm{MOG}})$ and $\Delta V_{\mathrm{p}}(e_{\mathrm{MOG}})$ for a_{MOG} = 1 AU.

Graphing both $\Delta V_{\mathrm{a}}(e_{\mathrm{MOG}})$ and $\Delta V_{\mathrm{p}}(e_{\mathrm{MOG}})$ for fixed a_{MOG} in Figure 8, it is evident that $\Delta V_{\mathrm{a}}(e_{\mathrm{MOG}}) \leq \Delta V_{\mathrm{p}}(e_{\mathrm{MOG}})$. Since the dependence of $\Delta V_{\mathrm{a}}(a_{\mathrm{MOG}}, e_{\mathrm{MOG}})$ and $\Delta V_{\mathrm{p}}(a_{\mathrm{MOG}}, e_{\mathrm{MOG}})$ on a_{MOG} is just a scaling factor of $1/\sqrt{a_{\mathrm{MOG}}}$:

$$\Delta V_{\mathrm{a}}(a_{\mathrm{MOG}}, e_{\mathrm{MOG}}) \leq \Delta V_{\mathrm{p}}(a_{\mathrm{MOG}}, e_{\mathrm{MOG}}) \quad \forall\, (a_{\mathrm{MOG}}, e_{\mathrm{MOG}}) \in \mathbb{R}_{+} \times (0, 1) \tag{11}$$

Note that we are only considering elliptical orbits, that is $0 \leq e_{\mathrm{MOG}} < 1$. The limits of ΔV_{a} and ΔV_{p} as e_{MOG} goes to 1 exist and are finite:

$$\begin{aligned} \lim_{e_{\mathrm{MOG}} \to 1} (\Delta V_{\mathrm{a}}(a_{\mathrm{MOG}}, e_{\mathrm{MOG}})) &= \sqrt{\frac{\mu_{\mathrm{sun}}}{a_{\mathrm{MOG}}}} \cdot (\sqrt{3} - 1) \\ \lim_{e_{\mathrm{MOG}} \to 1} (\Delta V_{\mathrm{p}}(a_{\mathrm{MOG}}, e_{\mathrm{MOG}})) &= \sqrt{\frac{\mu_{\mathrm{sun}}}{a_{\mathrm{MOG}}}} \end{aligned} \tag{12}$$

Thus the globally optimal ΔV for the 2-Burn MOG insertion transfer is ΔV_{a}, as defined in Equation (9). We present formulas for the transfer orbit time of flight (TOF) and the true anomaly difference between the shuttle and the center of the MOG formed by this 2-burn MOG orbital insertion process, $\Delta\theta$, as defined in Figure 6, in equations (13) and (14).

$$TOF_{2\mathrm{BI}} = \frac{1}{2} T_{\mathrm{transfer\_orbit}} = \pi \sqrt{\frac{(a_{\mathrm{MOG}} \cdot (1 + \frac{1}{2} e_{\mathrm{MOG}}))^3}{\mu_{\mathrm{sun}}}} \tag{13}$$

$$\Delta\theta_{2\mathrm{BI}} = \Delta\theta_{\mathrm{shuttle}} - \Delta\theta_{\mathrm{t.o.}} = 2\pi \cdot \frac{TOF_{2\mathrm{BI}}}{T_{\mathrm{MOG}}} - \pi = \pi \cdot \left([1 + \frac{1}{2} e_{\mathrm{MOG}}]^{\frac{3}{2}} - 1\right) \tag{14}$$

1-Burn Direct Insertion from a Circular Orbit

While the Hohmann Insertion strategy analyzed in the previous sub-section is the MOG insertion strategy that minimizes ΔV, it has a long flight time of $TOF_{2\text{BI}}$ – for reference, such an insertion maneuver for a_{MOG} = 1.25 AU and e_{MOG} = 0.3 has a time of flight of 315 Earth days, nearly a year.

Instead, we may consider a direct, 1-burn insertion from the shuttle circular orbit into the MOG elliptical orbit. Indeed, since the shuttle circular orbit and MOG elliptical orbits are coplanar and of same semi-major axis, they are guaranteed to intersect at two distinct points, plotted in Figure 9 for some $0 < e_{\text{MOG}} < 1$. By symmetry, the ΔV required to insert at each intersection is the same, so without loss of generality we can compute the ΔV of the intersection represented in Figure 9 as a function of e_{MOG}.

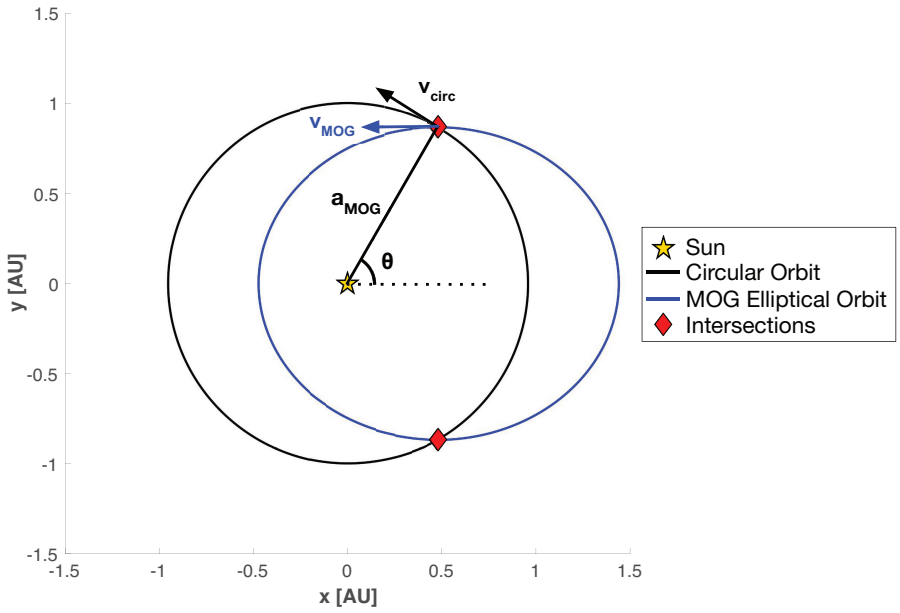

Figure 9: One-Burn Direct MOG Insertion Geometry. There are two intersections between the circular and MOG elliptical orbit: intersection 1, with y > 0, and intersection 2, with y < 0.

As represented in Figure 9, the intersection between an circle of radius a_{MOG} and an ellipse of semi-major axis a_{MOG} always occurs at the ellipse's semi-minor axis. We then have:

$$\theta = \arccos(a_{\text{MOG}}\ e_{\text{MOG}}/a_{\text{MOG}}) = \arccos(e_{\text{MOG}})$$

$$\Delta V_{1\text{BI}} = \|\vec{v}_{\text{circ}} - \vec{v}_{\text{MOG}}\| = \left\| \begin{bmatrix} -\sin(\theta)\sqrt{\frac{\mu_{\text{sun}}}{a_{\text{MOG}}}} + \sqrt{\frac{\mu_{\text{sun}}}{a_{\text{MOG}}}} \\ \cos(\theta)\sqrt{\frac{\mu_{\text{sun}}}{a_{\text{MOG}}}} \end{bmatrix} \right\| = \sqrt{\frac{\mu_{\text{sun}}}{a_{\text{MOG}}}}\sqrt{2(1-\sqrt{1-e_{\text{MOG}}^2})} \quad (15)$$

By construction, $TOF_{1\text{BI}} = 0 << TOF_{2\text{BI}}$. Now, let us consider the true anomaly difference $\Delta\theta_{1\text{BI}}$ between the shuttle on the circular orbit, and the center of the MOG constructed using this 1-burn insertion procedure. Employing a similar method as used in the previous section to find $\Delta\theta_{2\text{BI}}$, we obtain:

$$\Delta\theta_{1\text{BI}} = \pm(\frac{\pi}{2} + e_{\text{MOG}} - \theta) = \pm(\frac{\pi}{2} + e_{\text{MOG}} - \arccos(e_{\text{MOG}})) \tag{16}$$

The $\pm$ emerges from the possibility of direct, 1-burn injection at either of the intersections between the circular orbit and MOG elliptical orbit.

Tradeoffs of 2-Burn Insertion from a Circular Orbit: ΔV v/s TOF

The two MOG orbital insertion strategies considered so far clearly exemplify the trade-off between the ΔV and the time of flight TOF of the satellites' transfer from the circular deployment orbit to their final MOG elliptical orbits. The Hohmann transfer, or ΔV-optimal 2-Burn insertion, is the minimal-ΔV option, while the 1-Burn insertion analyzed in the previous subsection is the minimal TOF option.

To evaluate this tradeoff in further detail, for a range of e_{MOG} we minimize the ΔV of a 2-burn insertion maneuver of a predetermined time of flight $0 \leq TOF \leq TOF_{2\text{BI}}$. We used a similar approach to that presented in Algorithm 1: for some e_{MOG} and some fixed TOF, we discretize the terminal orbits and use the *lambert*() function to obtain the ΔV associated with a transfer of duration TOF between each pair of departure/arrival locations.

We plot the results of this optimization in Figure 10 for a range of e_{MOG} values and $a_{\text{MOG}} = 1$ AU. We observe that a local ΔV minimum, corresponding to the Hohmann transfer to the periapsis of the MOG orbit, offers a good compromise between satellite insertion ΔV and time of flight. To convert each data-point to ΔV and TOF necessary for the same transfer for a different a_{MOG}, simply scale the ΔV by a factor of $f_{\Delta\text{V}} = \sqrt{1/a_{\text{MOG}}}$ and the TOF by a factor of $f_{\text{TOF}} = \sqrt{a^3_{\text{MOG}}}$. We present the apoapsis Hohmann, periapsis Hohmann, and 1-burn insertion results for a larger number of MOG eccentricities in Appendix B.

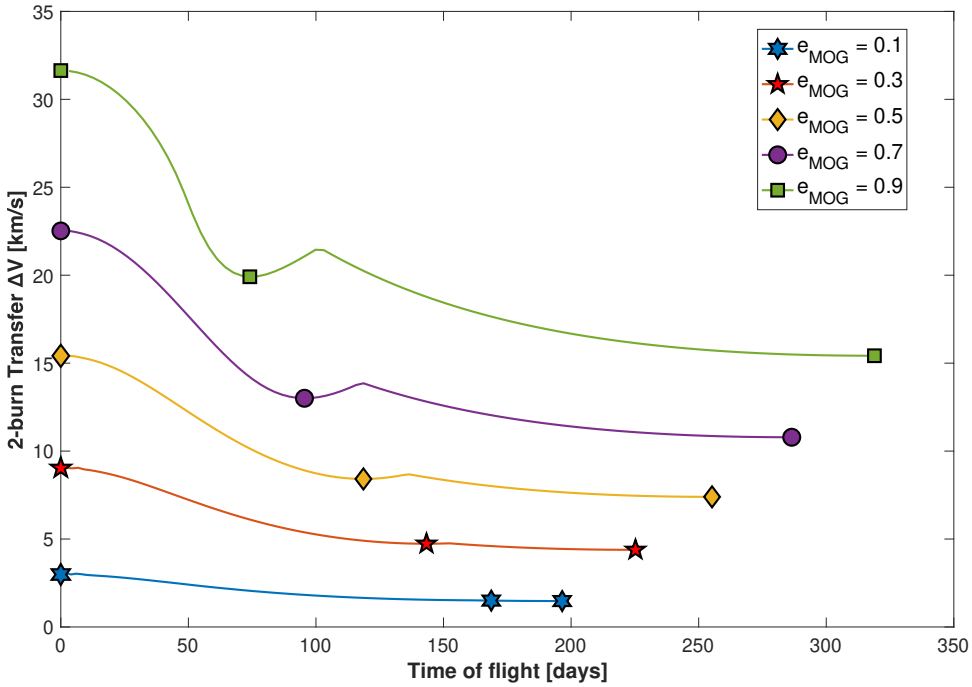

Figure 10: ΔV versus Time of Fight (TOF) for feasible 2-burn MOG Orbital Insertions, $a_{\text{MOG}} = 1$ AU. The markers on the y-axis are the 1-burn transfers ($TOF = 0$), while the right-most markers are the Hohmann transfer MOG insertions analyzed in the previous section. Finally, the central marker on each curve indicates a local ΔV minimum, corresponding to the periapsis Hohmann transfer discussed earlier.

Spread-out MOG Insertion

We also develop a MOG orbital insertion strategy reliant on MOG phase change maneuvers, outlined as follows:

1. MOG satellites launch to LEO, stowed in the payload bay of some launch vehicle
2. A bus containing the satellites (e.g., Starship upper stage) carries out burns to exit LEO, and carries out a Hohmann transfer to an elliptical orbit of semi-major axis a_{MOG} and eccentricity e_{MOG}: The bus is thereafter itself in the MOG.
3. From the bus' position in the MOG, the satellites fan out, changing their MOG phase to insert into their appropriate MOG orbits

We expect that this approach will be prohibitively expensive in ΔV for the MOG satellites for most a_{MOG} and e_{MOG}, as MOG phase changes near π radians are required for such a "spread out insertion" procedure. However, there are some combinations of MOG parameters, namely for large of small a_{MOG}, where this is offset by the shuttle's transfer being cheaper in the Spread-out Insertion procedure than in the Hohmann and 1-burn procedures.

In this spread-out insertion method, some satellites will have a larger insertion ΔV than others – we thus lose the convenient symmetry that simplified the analysis of previously considered MOG orbital insertion strategies. Let's assume that the mass of the structure of the MOG satellites' propellant tanks is small compared to the total wet mass of the satellites. Under this assumption, we model the "dry mass" of each satellite, or the mass of each satellite when it reaches its final MOG orbit, as all being equal, despite the dissymmetry in insertion ΔVs. The MOG satellites having identical dry masses is consistent with most Solar-orbiting MOG use cases, such as interplanetary communications constellations and astrophysics experiments, because such applications generally use identical satellites.

For a total shuttle payload mass of m_{payload}, we have:

$$m^d_{\mathrm{persat}} = \frac{m_{\mathrm{payload}}}{\sum_{i=1}^{N_{\mathrm{sats}}} (\exp(\Delta V_{\mathrm{i}}/I_{sp}g_0))} \tag{17}$$

where m^d_{persat} is the dry mass per satellite delivered into the MOG orbit for those MOG parameters and that number of satellites.

The exponential relationship between ΔV_{i} and the corresponding fuel expense of each term of the sum in Equation (17) is derived from the Tsiolkovsky rocket equation. This exponential relationship also makes it so that the sum of satellite propellant masses is dominated by the contribution of the largest ΔV_{i} – therefore, to maximize m^d_{persat}, we must find the distribution of ΔV_{i} that minimizes $\max_{i=1,..,N_{\mathrm{sats}}}(\Delta V_{\mathrm{i}})$.

This is equivalent to finding, for a given N_{sats}, the distribution of $\Delta\phi_{\mathrm{MOG}}$, assigned to the satellites to "spread out" from the shuttle into their MOG orbits, that minimizes $\max_{i=1,..,N_{\mathrm{sats}}}(\Delta V_{\mathrm{i}})$. As we derived in the MOG Phasing section, the function relating ΔV to $\Delta\phi$ is nearly parabolic. Since the $\Delta\phi_{\mathrm{i}}$s need to have an even spacing of $2\pi/N_{\mathrm{sats}}$, we obtain the distribution of MOG phase changes described in Equation (18) and exemplified in Figure 11.

$$\Delta\phi_{\mathrm{MOG_i}} = \begin{cases} (i-1)\cdot\frac{2\pi}{N_{\mathrm{sats}}} & \text{if } N_{\mathrm{sats}} \text{ is odd} \\ \left(i-\frac{1}{2}\right)\cdot\frac{2\pi}{N_{\mathrm{sats}}} & \text{if } N_{\mathrm{sats}} \text{ is even} \end{cases} \quad \text{for } i = 1,\ldots,N_{\mathrm{sats}} \tag{18}$$

We expect that this insertion procedure will under-perform in most situations compared to the Hohmann insertion procedure due to the large ΔV associated with the insertion of the satellites making ϕ_{MOG} changes of nearly π radians, and the exponential relationship between propellant expenditure and ΔV requirements. However, we also expect that inserting the shuttle directly into the MOG will be less expensive than the

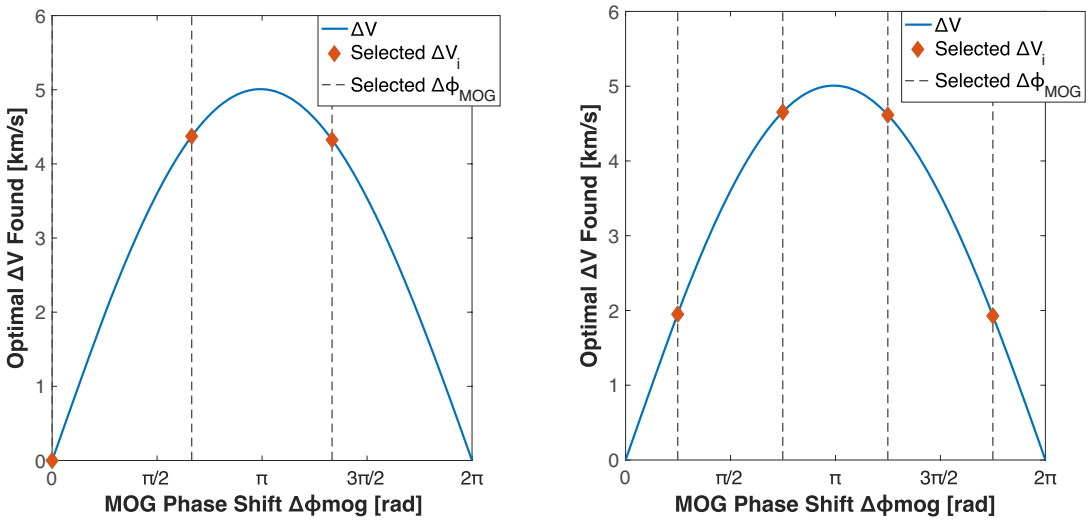

(a) $N_{\text{sats}} = 3$ (b) $N_{\text{sats}} = 4$

Figure 11: Attribution of $\Delta\phi_{\text{MOG}}$ for $N_{\text{sats}} = 3$ and $N_{\text{sats}} = 4$ as described in Equation (18). The maximum ΔV_{i} is minimized by relying on the ΔV distribution being close to that of a parabola centered at π radians. Odd numbers of satellites enable one satellite to remain by the shuttle and expend no ΔV.

shuttle undergoing a Hohmann transfer to a circular orbit of radius a_{MOG}, as is the case in the 2-burn insertion procedures analyzed in previous sections.

However, the dry mass per satellite delivered to the MOG using this spread-out insertion strategy (Equation (17)) depends on the specific impulse of the thrusters used by the MOG satellites to conduct their impulsive maneuvers. To quantitatively compare the different MOG insertion procedures presented and analyzed in this paper, we consider an applied deployment scenario where these maneuvers are conducted by spacecraft with representative values for parameters such as shuttle payload capacity, the specific impulse of the shuttle's propulsion system, and the specific impulse of the satellites' thrusters.

MOG Insertion Evaluation – Full Deployment Scenario with a Specific Launch Vehicle

To ground the different MOG insertion strategies in reality, we evaluate their feasibility using a specific launch vehicle and realistic assumptions about the satellites' propulsion capabilities. For this analysis, we select SpaceX's Starship upper stage paired with the Super Heavy booster. This vehicle is chosen due to its large payload capacity to Low Earth Orbit (LEO), full reusability, and increasing adoption in mission concepts and proposals.[19]

Table 2 summarizes key performance metrics for three iterations of Starship, compiled by Ars Technica[20] from both SpaceX's website[21] and public announcements made by SpaceX officials.

Table 2: Starship Performance Metrics[20,21]

Starship Metrics	Block I	Block II	Block III
Payload to LEO (t)	N/A	100	200
Ship Propellant Load (t)	1200	1500	2300
Ship Dry Mass (t)	100	116	160

We use the Block III version of the Starship launch vehicle, as it is the most recent iteration of the design.

Additionally, for all of Starship's propulsive maneuvers outside of the Earth's atmosphere we use the specific impulse (Isp) of Starship's Raptor vacuum thruster: 382 s in vacuum.[22] For the satellites' onboard propulsion systems, we choose a specific impulse of 300 s, which corresponds to a typical specific impulse of the main engines of interplanetary spacecraft, such as Galileo's 400 N monomethylhydrazine and nitrogen tetroxide main engine.[23]

We assume the following launch procedure:

1. Starship launches carrying up to 200 metric tonnes of satellites, entering a parking orbit in LEO.
2. Starship is refuelled in LEO by reusable tankers, similar to the concept of operations of the Artemis missions.
3. Starship executes a burn to enter a hyperbolic trajectory exiting the Earth's Sphere of Influence (SOI) with a hyperbolic asymptotic velocity v_∞ that places it in the appropriate Hohmann transfer orbit.
4. Starship regularizes its orbit into the orbit from which the MOG satellites are deployed – a circular orbit a $R = a_{\mathrm{MOG}}$ for the 2-burn insertion procedures, and a MOG elliptical orbit for the spread-out insertion procedure.
5. The MOG satellites insert into their MOG orbits following the MOG insertion procedure for that deployment scenario.

Figures 12, 13, and 14 show the results of the analysis for the Hohmann insertion procedure, 1-Burn insertion procedure, and Spread-out insertion procedure respectively. We conducted the analysis for $N_{\mathrm{sats}} = 10$ and used a logarithmic color scale to represent the satellite dry mass at some a_{MOG}, e_{MOG}.

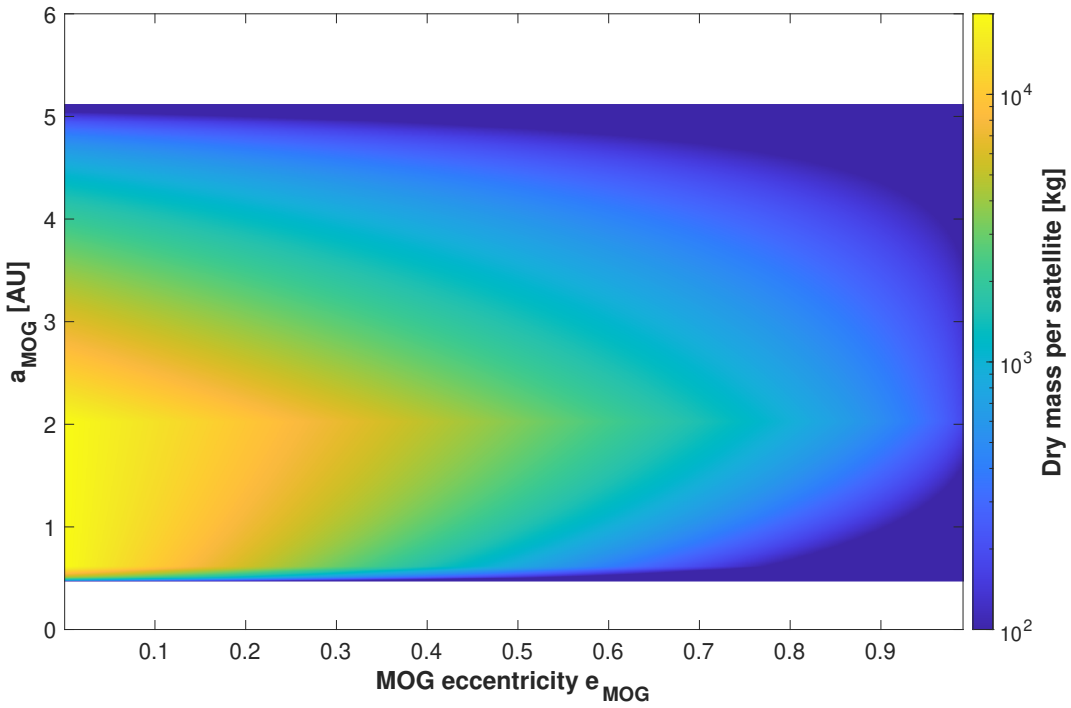

Figure 12: MOG Satellite Dry Mass with $N_{\mathrm{sats}} = 10$, Hohmann Transfer MOG Insertion

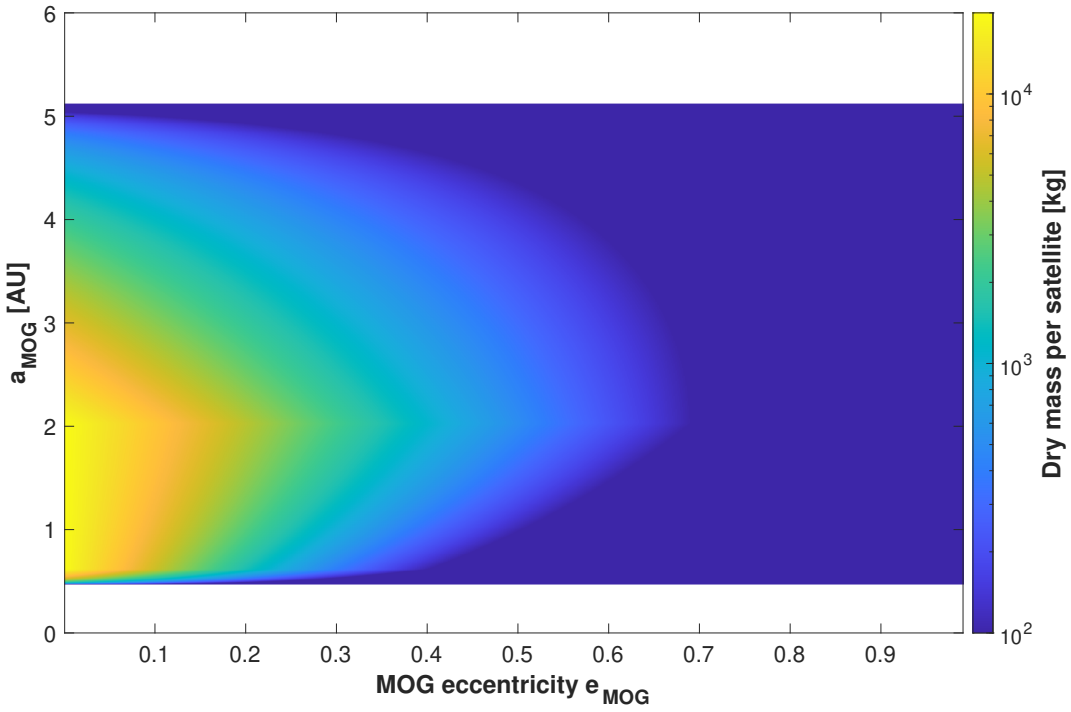

Figure 13: MOG Satellite Dry Mass with $N_{\text{sats}} = 10$, 1-Burn MOG Insertion

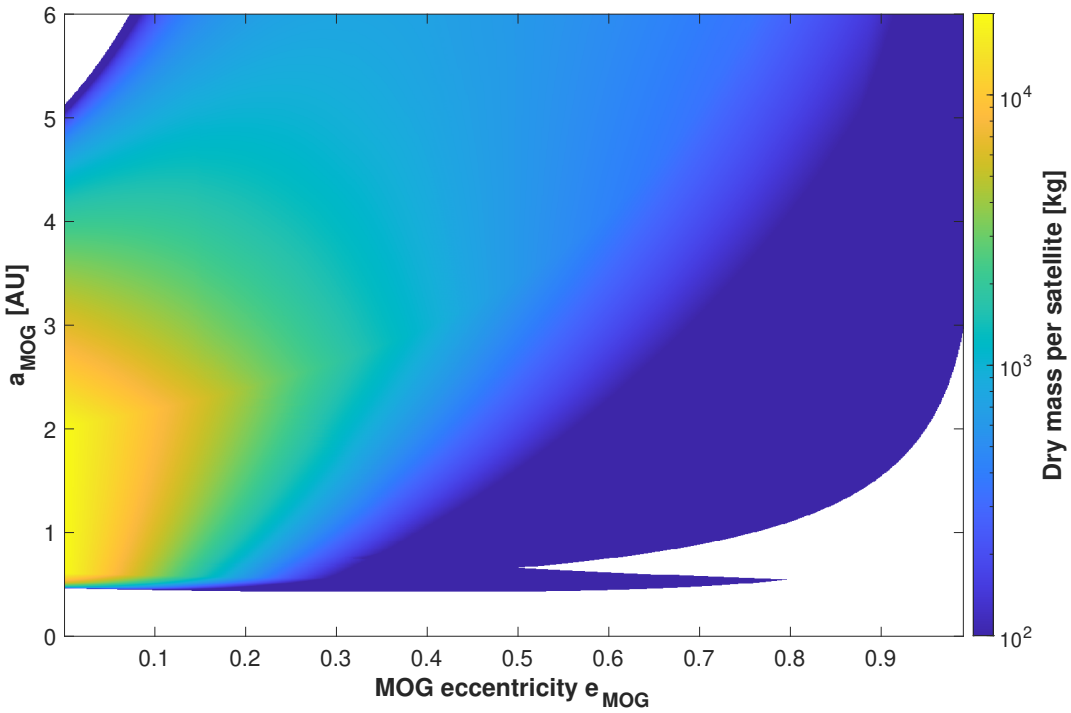

Figure 14: MOG Satellite Dry Mass with $N_{\text{sats}} = 10$, Spread-out MOG Insertion

The Hohmann transfer and 1-Burn transfer procedures both have a feasible range of MOG semi-major axes a_{MOG} of approximately 0.47-5.12 AU. Beyond those bounds, the Starship vehicle is no longer capable of transferring a non-zero payload mass into the circular orbit of radius a_{MOG}, leading to the infeasible region visible in Figures 12 and 13. Within the feasible region, as expected the dry mass of each satellite delivered to the MOG decreases with increasing MOG eccentricity. Also as expected, the Hohmann Transfer MOG Insertion Procedure outperforms the 1-Burn MOG Insertion procedure for all their feasible a_{MOG}, e_{MOG}. The Hohmann Transfer MOG Insertion procedure also clearly outperforms the Spread-out MOG Insertion (SI) procedure for a_{MOG} in the 0.5-3.5 AU range, which stems from how expensive the SI procedure's satellite MOG phasing maneuvers are compared to a Hohmann transfer.

The Spread-out Insertion procedure has a more complex feasible region than the Hohmann and 1-Burn Insertion procedures. This is due to the SI procedure dictating that the Starship insert itself into a MOG elliptical orbit – for large or small a_{MOG}, and non-zero e_{MOG}, having the shuttle insert directly into a MOG elliptical orbit requires less ΔV than inserting into a circular orbit of radius a_{MOG} (as is required by the other insertion procedures). This leads to an extended feasible region past the a_{MOG} limits of the other insertion procedures: for instance, the SI procedure can even insert ten 1,977 kg satellites into a MOG of eccentricity 0.6 and semi-major axis 39.44 AU – the semi-major axis of Pluto's orbit around the Sun.

This analysis shows that the fuel-optimal insertion procedure for most MOGs with a_{MOG} in the 0.5-3.5 AU range is the Hohmann Transfer MOG Insertion procedure, while the Spread-out MOG Insertion procedure performs better for large a_{MOG}. Regardless, clearly it is possible to construct planar MOGs in Solar orbit for a wide range of MOG parameters. For example, with just one Starship it is possible to insert ten 10,000 kg spacecraft into a MOG with (a_{MOG}, e_{MOG}) = (2.0 AU, 0.3), or even three spacecraft of dry mass 63,380 kg into the planar version of the proposed LISA[7] MOG formation ($e_{\mathrm{MOG}} \approx 0.01$, $a_{\mathrm{MOG}} = 1$ AU).

CONCLUSION

Mutually Orbiting Groups (MOGs) enable new classes of space missions, from distributed science observatories[7,8] to interplanetary communication networks.[9] In this paper, we examined heliocentric planar MOGs, which we characterized according to three parameters: the MOG semi-major axis a_{MOG}, the MOG eccentricity e_{MOG}, and the number of MOG satellites N_{sats}. We developed a general methodology to quantify the propulsive requirements of MOG orbital insertion and phasing maneuvers as a function of these MOG parameters.

Although large MOG phase changes remain expensive, we demonstrated the feasibility of small satellite position adjustments within the MOG, with propulsive costs on the order of km/s per radian. These fuel-optimal two-burn phasing maneuvers enable the dynamic reconfiguration of MOG formations, supporting satellite replacements and additions to the formation.

We proposed and analyzed three distinct MOG orbital insertion strategies, finding that the Hohmann transfer provides the lowest-ΔV insertion, whereas the 1-burn transfer minimizes the insertion time. Meanwhile, we developed the spread-out insertion procedure to broaden the range of feasible a_{MOG}. To meaningfully compare these MOG insertion strategies, we modeled a full deployment scenario using realistic propulsion system performance estimates for the launch vehicle and MOG satellites. Our results showed that the total dry mass per satellite is highly sensitive to both the MOG parameters and the selected orbital insertion strategy.

The approach we have developed provides mission designers with a generalizable tool for planning the deployment and reconfiguration of planar heliocentric MOGs. Future work would explore alternative orbital insertion and phasing strategies, such as multi-burn maneuvers or low-thrust propulsion, to further reduce shuttle ΔV and extend the range of feasible MOG configurations. Furthermore, our analysis can be extended to cover inclined solar-orbiting, Earth-orbiting, and planetary MOGs, further broadening their potential applications in distributed space systems. Finally, this work can be generalized to the broader family of 2D planar flower constellations, extending our deployment and phasing methods to the various constellation structures that emerge from different relative spacings of satellites' mean anomalies and arguments of periapsis.

ACKNOWLEDGMENTS

J. Pénot was supported by the National Science Foundation Graduate Research Fellowship under Grant No. 2024377105. This work was also supported in part by NASA under Grant No. 80NSSC23M0220. Any opinions, findings, conclusions, or recommendations expressed in this material are those of the authors and do not necessarily reflect the views of the National Science Foundation or any NASA entity.

NOTATION

α_+	marginal ΔV cost of small positive MOG phasing maneuvers
α_-	marginal ΔV cost of small negative MOG phasing maneuvers
a_{MOG}	MOG semi-major axis
AU	Astronomical Unit, Earth's average distance from the Sun
e_{MOG}	MOG eccentricity
ΔV	delta-V, a measure of the impulse per unit of spacecraft mass needed to perform a maneuver
ω	argument of periapsis
M	mean anomaly
M_{MOG}	MOG mean anomaly
MOG	Mutually Orbiting Group
μ_{sun}	the Sun's standard gravitational parameter
N_{sats}	number of satellites in a MOG
ϕ_{MOG}	MOG phase
PNT	Positioning, Navigation, and Timing
RAAN	Right Ascension of the Ascending Node
θ	true anomaly
TOF	time of flight

REFERENCES

[1] D. Selva, A. Golkar, O. Korobova, I. L. i. Cruz, P. Collopy, and O. L. d. Weck, "Distributed Earth Satellite Systems: What Is Needed to Move Forward?," *Journal of Aerospace Information Systems*, Vol. 14, No. 8, 2017, pp. 412–438, 10.2514/1.I010497.

[2] J. Alvarez and B. Walls, "Constellations, clusters, and communication technology: Expanding small satellite access to space," *2016 IEEE Aerospace Conference*, 2016, pp. 1–11, 10.1109/AERO.2016.7500896.

[3] R. Fitzgerald, L. Halperin, S. Leroy, A. Gagnon, K. Cahoy, and J. Clark, "Analyzing Constellation Performance for the Radio Occultation Tomography of Internal Gravity Waves," *IEEE Journal of Selected Topics in Applied Earth Observations and Remote Sensing*, Vol. 14, 2021, pp. 7225–7236. Conference Name: IEEE Journal of Selected Topics in Applied Earth Observations and Remote Sensing, 10.1109/JSTARS.2021.3080984.

[4] S. C. Burleigh, T. De Cola, S. Morosi, S. Jayousi, E. Cianca, and C. Fuchs, "From Connectivity to Advanced Internet Services: A Comprehensive Review of Small Satellites Communications and Networks," *Wireless Communications and Mobile Computing*, Vol. 2019, No. 1, 2019, p. 6243505. _eprint: https://onlinelibrary.wiley.com/doi/pdf/10.1155/2019/6243505, 10.1155/2019/6243505.

[5] T. Zhang, Y. Qian, C. Li, J. Lu, J. Fu, Q. Guo, S. Guo, and Y. Wang, "Imaging and Interferometric Mapping Exploration for PIESAT-01: The World's First Four-Satellite "Cartwheel" Formation Constellation," *Atmosphere*, Vol. 15, June 2024, p. 621. Number: 6 Publisher: Multidisciplinary Digital Publishing Institute, 10.3390/atmos15060621.

[6] J. Schoolcraft, A. Klesh, and T. Werne, "MarCO: Interplanetary Mission Development on a CubeSat Scale," *Space Operations: Contributions from the Global Community* (C. Cruzen, M. Schmidhuber, Y. H. Lee, and B. Kim, eds.), pp. 221–231, Cham: Springer International Publishing, 2017, 10.1007/978-3-319-51941-8_10.

[7] S. Marmori and A. Morselli, "Fuel-optimal acquisition and control of a cartwheel formation in Earth displaced heliocentric orbit," *Advances in Space Research*, Vol. 74, Nov. 2024, pp. 4948–4967, 10.1016/j.asr.2024.08.073.

[8] W.-R. Hu and Y.-L. Wu, "The Taiji Program in Space for gravitational wave physics and the nature of gravity," *National Science Review*, Vol. 4, Sept. 2017, pp. 685–686, 10.1093/nsr/nwx116.

[9] M. B. Quadrelli, R. Hodges, V. Vilnrotter, S. Bandyopadhyay, F. Tassi, and S. Bevilacqua, "Distributed Swarm Antenna Arrays for Deep Space Applications," *2019 IEEE Aerospace Conference*, Mar. 2019, pp. 1–15. ISSN: 1095-323X, 10.1109/AERO.2019.8742019.

[10] Y. Xia, G. Li, G. Heinzel, A. Rüdiger, and Y. Luo, "Orbit design for the Laser Interferometer Space Antenna (LISA)," *Science China Physics, Mechanics and Astronomy*, Vol. 53, Jan. 2010, pp. 179–186, 10.1007/s11433-010-0100-7.

[11] W. Martens and E. Joffre, "Trajectory Design for the ESA LISA Mission," *The Journal of the Astronautical Sciences*, Vol. 68, June 2021, pp. 402–443. arXiv:2101.03040 [gr-qc], 10.1007/s40295-021-00263-2.

[12] D. Mortari, M. P. Wilkins, and C. Bruccoleri, "The Flower Constellations," *The Journal of the Astronautical Sciences*, Vol. 52, Mar. 2004, pp. 107–127, 10.1007/BF03546424.

[13] R. Oldenhuis, "MATLAB Robust solver for Lambert's orbital-boundary value problem," https://github.com/rodyo/FEX-Lambert/releases/tag/v1.4, 2009. Accessed: December 12, 2024.

[14] D. Izzo, "Revisiting Lambert's problem," *Celestial Mechanics and Dynamical Astronomy*, Vol. 121, Jan. 2015, pp. 1–15, 10.1007/s10569-014-9587-y.

[15] Lancaster and Blancard, "A unified form of lambert's theorem," *NASA technical note TN D-5368*, 1969.

[16] R. H. Gooding, "A procedure for the solution of Lambert's orbital boundary-value problem," *Celestial Mechanics and Dynamical Astronomy*, Vol. 48, June 1990, pp. 145–165, 10.1007/BF00049511.

[17] M. Pontani, "Simple Method to Determine Globally Optimal Orbital Transfers," *Journal of Guidance, Control, and Dynamics*, Vol. 32, May 2009, pp. 899–914, 10.2514/1.38143.

[18] D. Vallado, *Fundamentals Of Astrodynamics And Applications*. Microcosm Press, 4th ed., 2013.

[19] M. Knapp, L. Paritsky, E. Kononov, and M. M. Kao, "Great Observatory for Long Wavelengths (GO-LoW) NIAC Phase I Final Report," Apr. 2024. arXiv:2404.08432 [astro-ph], 10.48550/arXiv.2404.08432.

[20] E. Berger, "Elon Musk just gave another Mars speech—this time the vision seems tangible," https://arstechnica.com/space/2024/04/elon-musk-just-gave-another-mars-speech-this-time-the-vision-seems-tangible/, 2024. Accessed: March 26, 2025.

[21] SpaceX, "Starship: Service to Earth Orbit, Moon, Mars and Beyond," https://www.spacex.com/vehicles/starship/, 2025. Accessed: March 26, 2025.

[22] E. Musk, "Making Humans a Multi-Planetary Species," *New Space*, Vol. 5, 2017.

[23] T. Barber, F. Krug, K. Renner, T. Barber, F. Krug, and K. Renner, "Final Galileo Propulsion System in-flight characterization," *33rd Joint Propulsion Conference and Exhibit*, Seattle,WA,U.S.A., American Institute of Aeronautics and Astronautics, July 1997, 10.2514/6.1997-2946.

APPENDIX A: NORMALIZED MOG PROFILES AS A FUNCTION OF MOG ECCENTRICITY

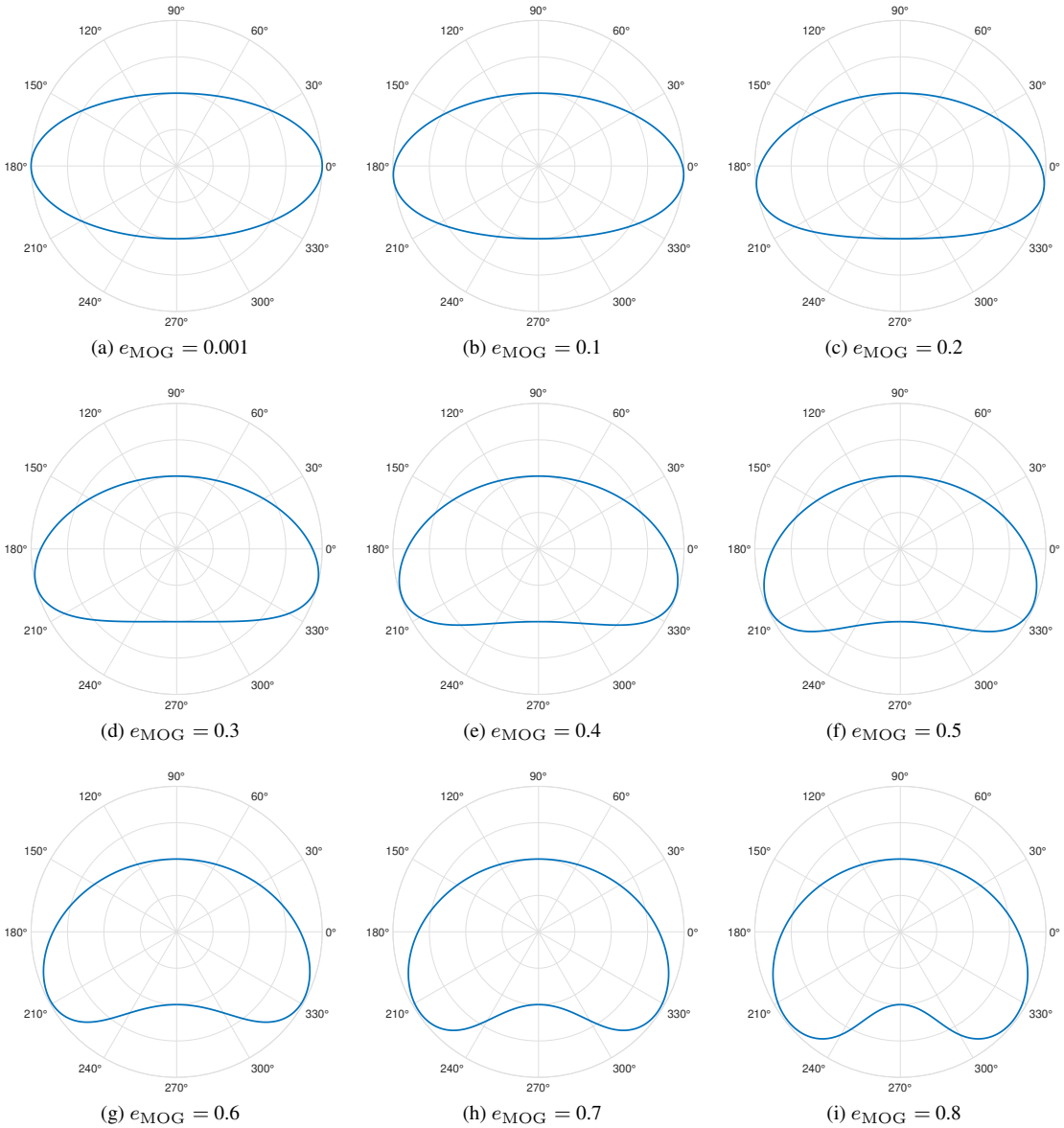

(a) $e_{\mathrm{MOG}} = 0.001$ (b) $e_{\mathrm{MOG}} = 0.1$ (c) $e_{\mathrm{MOG}} = 0.2$

(d) $e_{\mathrm{MOG}} = 0.3$ (e) $e_{\mathrm{MOG}} = 0.4$ (f) $e_{\mathrm{MOG}} = 0.5$

(g) $e_{\mathrm{MOG}} = 0.6$ (h) $e_{\mathrm{MOG}} = 0.7$ (i) $e_{\mathrm{MOG}} = 0.8$

Figure A1: Normalized MOG Profiles of Various Eccentricities. A planar MOG of small eccentricity forms a nearly-perfect ellipse of eccentricity $\sqrt{3}/2$, but this elliptical shape is deformed as e_{MOG} increases.

APPENDIX B: DATA FROM THE ΔV VERSUS TOF TRADEOFF ANALYSIS

Table B1: Data from the ΔV versus TOF Tradeoff Analysis. Time of flights (TOF) are in days, and ΔV are in km/s.

e_{MOG}	1-burn ΔV	Hohmann TOF	Hohmann ΔV	Local Min. TOF	Local Min. ΔV
0.05	1.49	189.5	0.74	175.8	0.75
0.1	2.98	196.5	1.47	169.1	1.51
0.15	4.48	203.6	2.20	162.5	2.29
0.2	5.99	210.7	2.93	155.9	3.08
0.25	7.51	217.9	3.66	149.7	3.89
0.3	9.04	225.2	4.39	143.3	4.73
0.35	10.59	232.6	5.12	136.3	5.60
0.4	12.17	240.1	5.87	131.0	6.50
0.45	13.78	247.6	6.62	125.1	7.43
0.5	15.42	255.2	7.40	118.6	8.42
0.55	17.10	262.9	8.19	111.5	9.45
0.6	18.84	270.7	9.01	106.6	10.55
0.65	20.64	278.5	9.88	101.3	11.73
0.7	22.52	286.5	10.79	95.5	13.00
0.75	24.51	294.4	11.76	89.2	14.40
0.8	26.64	302.5	12.82	85.6	15.96
0.85	28.98	310.7	14.02	78.4	17.76
0.9	31.64	318.9	15.42	74.1	19.92
0.95	34.93	327.2	17.25	69.4	22.76

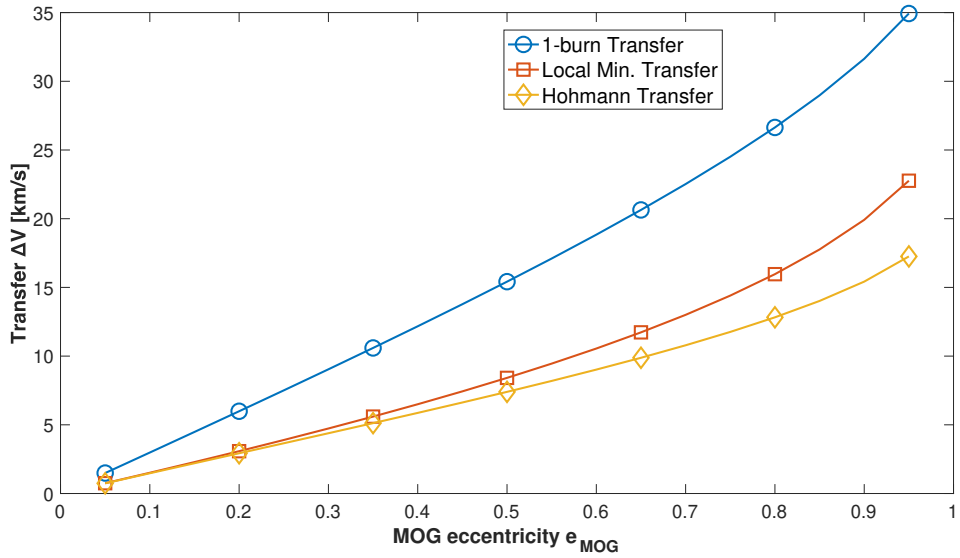

Figure B1: Plot of ΔV Data as a function of MOG eccentricity e_{MOG}. Data included in Table B1.

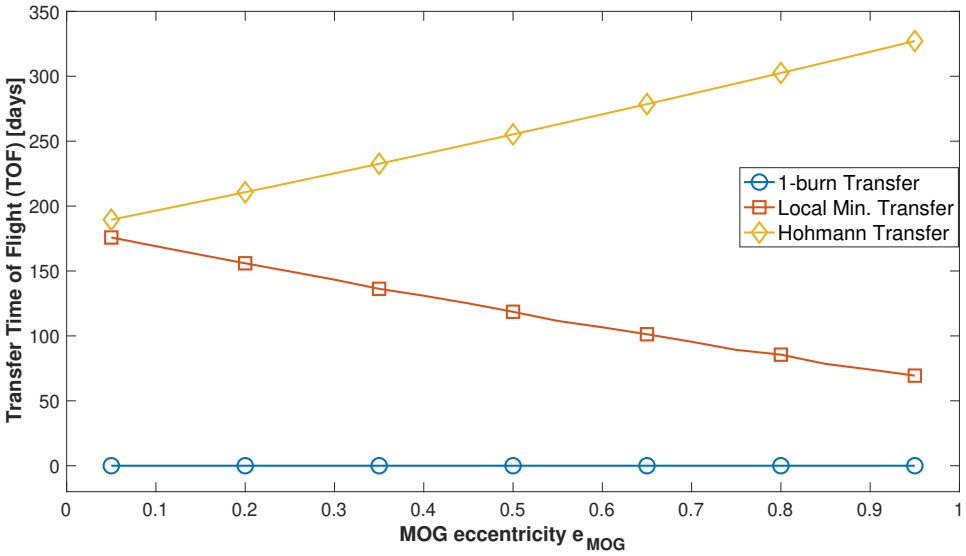

Figure B2: Plot of Time of Flight (TOF) Data as a function of MOG eccentricity e_{MOG}. TOF for the 1-burn insertion is 0 by construction. Data included in Table B1.